High-temperature oxidation behavior of additively manufactured IN625: Effect of microstructure and grain size

Corrosion Science 205 (2022) 110382

Contents lists available at ScienceDirect

Corrosion Science

journal homepage: www.elsevier.com/locate/corsci

High-temperature oxidation behavior of additively manufactured IN625: Effect of microstructure and grain size

Anton Chyrkin [a], Kerem O. Gunduz [a,b], Irina Fedorova [c], Mohammad Sattari [c], Alberto Visibile [a], Mats Halvarsson [c], Jan Froitzheim [a,*], Krystyna Stiller [c]

[a] Chalmers University of Technology, Department of Chemistry and Chemical Engineering, Kemivägen 10, SE-41296 Gothenburg, Sweden
[b] Gebze Technical University, Department of Materials Science and Engineering, 41400 Gebze, Kocaeli, Turkey
[c] Chalmers University of Technology, Department of Physics, Kemigården 1, SE-41296 Gothenburg, Sweden

ARTICLE INFO

Keywords:
High-temperature oxidation
Ni-base alloys
IN625
Additive manufacturing
SLM
Intergranular corrosion

ABSTRACT

High-temperature oxidation of additively manufactured (AM) Ni-base alloy IN625 has been studied in air and Ar-5%H_2-3%H_2O at 900–1000 °C. AM material is found to oxidize faster than the conventionally manufactured (CM) IN625 due to severe intergranular oxidation observed in the former. The AM IN625 was heat treated at 1100–1250 °C and hot rolled at 980 °C in order to modify the AM microstructure, primarily grain size, and analyze its role in alloy oxidation behavior. Grain size is shown to affect overall oxidation kinetics but not the intergranular oxidation morphology.

1. Introduction

Materials designed for applications at elevated temperatures in corrosive environments, e.g., aerospace technology, jet-engines and stationary gas turbines, offshore industries, heat processing and furnace linings etc., must provide good creep strength as well as corrosion resistance at high temperatures [1]. Ni-base superalloys remain up to date a superior commercial material of choice for these applications still outperforming emerging high-temperature alloys such as refractories [2], high-entropy alloys [3], Co-base γ/γ'-superalloys [4,5] and alumina-forming austenites [6]. Their oxidation/corrosion resistance relies on their ability to exclusively form external, protective Cr_2O_3 and/or Al_2O_3 oxide scales on the surface of components [7].

Wrought Ni-based alloy Inconel 625 (IN625) was developed in the 1960 s as a novel, high-strength steam-line piping material [8]. Further modifications were undertaken to improve creep-resistance and weldability of IN625 [9,10] resulting eventually in the development of IN718, the most spread Ni-base alloy in the aeronautic technology [11]. Alloyed by Mo, Nb and Cr, original IN625 provides an optimum combination of creep as well as corrosion resistance expanding its application field to numerous industries with temperatures ranging from cryogenic to around 1000 °C [12–15].

Very good mechanical properties of Ni-base superalloys attract industries to fabricate components from them using additive manufacturing (AM) technologies [16]. Additive manufacturing is the layer-by-layer formation of a 3D-material based on a computer design [17–19]. Compared to conventional manufacturing methods such as casting or forging, additive manufacturing has more freedom in the component design providing the production of very complex-shaped geometries without relying on secondary manufacturing processing techniques such as welding or machining [16]. Powder bed fusion (PBF) is a subset of AM in which powders are melt and fused by employing a laser (SLM: selective laser melting) or an electron beam (EBM: electron beam melting) in a powder bed system.

In the SLM technique, layer thickness values range from 20 to 100 μm [20]. Contrary to EBM, SLM eliminates the need for vacuum, is more versatile in terms of material selection, provides high cooling rates thus allows the formation of a fine-grained microstructure and easy removal of powder, better surface finish [21,22]. The AM alloy printing has two important features: fast cooling rates and directional solidification. In addition to scanning parameters such as beam size, scanning speed, hatch distance, energy density of the laser, powder characteristics such as purity, powder particle size distribution and morphology may also affect the end properties on an AM alloy, e.g., surface finish [20,23].

Although the microstructure of AM alloys strongly depends on the AM process type, numerous similarities were found in several studies on AM IN625 [24–31]. Both EBM and SLM deposition techniques produce a columnar grain structure of IN625 along the build direction [24–26].

* Corresponding author.
E-mail address: jan.froitzheim@chalmers.se (J. Froitzheim).

https://doi.org/10.1016/j.corsci.2022.110382
Received 21 December 2021; Received in revised form 16 April 2022; Accepted 12 May 2022
Available online 17 May 2022

The dendritic microstructure within the columns aligned to the build axis was found along with Ni_3Nb precipitates decorating these dendritic lines [27,28]. Nano-sized Ni_3Nb precipitates (about 50 nm) grow into needle-shaped precipitates with an average length of 1 μm during exposure at 870 °C for 1 h [27]. The AM production route of IN625 resulting in a textured microstructure leads to anisotropic mechanical properties, primarily hardness [27,30,31].

Much effort has recently been dedicated to a better understanding of the effect of AM microstructure on the high-temperature oxidation behaviour of the Ni-base alloys [32–41], including alloy IN625 [33,36, 39,41–44]. Most authors agree on three important facts: i) AM high-temperature alloys oxidize faster than their CM versions; ii) structural anisotropy has a limited effect on oxidation kinetics; iii) the origin of higher corrosion attack in AM alloys, mainly intergranular oxidation, is still not well understood. The data on AM high-temperature alloys generated and reported up to date still cannot provide a conclusive answer to the fundamental question: are these differences in oxidation behaviour governed by a specific AM microstructure or rather minor deviations in chemical composition resulting from the AM process?

The ambition of the present work is to elucidate the role of the AM microstructure, specifically grain size and texture, in oxidation behaviour of an SLM manufactured alloy IN625. The AM material was compared with a hot-forged IN625 (CM IN625) as well as heat treated and hot rolled versions of the same AM IN625 in order to retain the original chemical composition of AM material while changing its grain structure.

2. Experimental

2.1. Materials

Cubes of AM IN625 measuring 15×15×15 mm^3 were additively manufactured by SLM and provided by Siemens Energy AB (Finspång, Sweden) in the as-built condition. In order to analyze the microstructural anisotropy of the obtained AM material, the AM IN625 cubes were sectioned in 2 directions: parallel (AM-X and AM-Y) and perpendicular (AM-Z) to the build axis (see Fig. 1). As no differences between the longitudinal X and Y cuts were detected, both in parallel to the build direction, hereinafter only AM-Y is compared vs the transversal AM-Z cut.

The chemical composition of AM IN625 obtained by SEM-EDS is given in Table 1. It should be noted that carbon is beyond detection limit of the SEM-EDS technique. The conventionally manufactured (CM) alloy IN625 was a forged bar supplied by Huntington Alloy Corp. The same CM alloy batch was studied in [13]. The chemical composition of CM IN625 obtained by ICP-OES and IR spectroscopy for carbon [13] is also given in the Table 1.

Heat treatments of AM IN625 to remove the original AM microstructure and obtain bigger grains were carried out at 1100, 1200 and 1250 °C in vacuum (10^{-5} mbar). The sectioned alloy coupons were sealed in evacuated quartz ampullas and annealed in a tube furnace for 24 h at 1200 °C (AM-HT1), 200 h at 1100 °C (AM-HT2) and 100 h at 1250 °C (AM-CG), respectively, and quenched in water. The heat treatment parameters such as temperature and duration were selected to obtain a moderate (up to 100 μm) and very large grain size (some millimeters) [45]. The latter specimens were literally bicrystals having only one single grain boundary per 10 mm wide cross-sections.

3 AM IN625 cubes were hot rolled by HMW Hauner GmbH (Röttenbach, Germany). The as-built AM alloy cubes were heated to 980 °C and rolled to 2.5 mm thickness.

The alloy coupons of all IN625 variants were machined to 15×15×2 or 20×10×2 mm^3 dimensions. The surfaces were ground with SiC papers and polished to 0.25 μm with diamond pastes. Table 2 summarizes the different materials and heat treatments investigated in this study.

2.2. Exposures

Isothermal exposures were performed in tube furnaces (⌀ 44 mm) at 800–1000 °C under 1000 sml/min flow rate for up to 300 h in laboratory air. The specimens, degreased in ethanol and acetone prior to exposure, were directly introduced into the hot zone of the tube furnace. The temperature calibration was performed by an external Pt/Rh-thermocouple placed next to the specimens. After exposures, the specimens were removed from the hot zone of the furnace and cooled down in air. The mass gains curves were obtained by gravimetric measurements prior and after the exposures using Mettler Toledo XP6 microbalance with a 1 μg resolution. Each thermogravimetric measurement corresponds to an individual isothermal exposure without re-heating the same sample.

The exposures in Ar-5%H_2-3%H_2O were performed in a closed, gas-tight quartz tube. The Ar-5%H_2 gas mixture supplied by Linde gas was bubbled through a humidifier kept at 24.4 °C to obtain 3% absolute humidity (30 mbar of H_2O). The flow rate of the humidified gas was 200 sml/min. Unlike the air exposures, the specimens were introduced into a cold furnace, flushed with the gas mixture for 1 h and heated at 10 °C per minute to reach 900 °C. The cooling rate was 10 °C per minute as well.

2.3. Microstructural characterization

A Siemens D5000 X-ray diffractometer (Cu Kα radiation) was

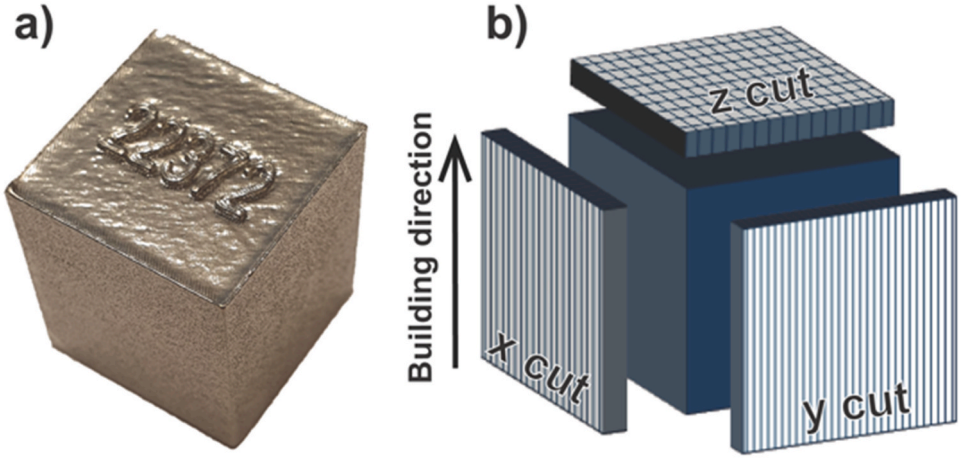

Fig. 1. AM IN 625: additively manufactured cube (a), schematic of sample cuts (b).

Table 1
Chemical composition of CM IN625 and AM IN625 in wt%.

Material	Ni	Cr	Mo	Fe	Nb	Al	Mn	Si	C
AM IN625	Bal.	21.49	8.7	0.8	3.9	0.3	0.1	0.12	DL*
CM IN625	Bal.	21.6	8.9	3.6	3.5	0.3	0.11	0.25	0.02

*DL – detection limit

Table 2
Overview of materials and heat treatments used in this study.

AM IN625	Additively manufactured INCONEL 625 in the as-built condition
AM-Y	Y-cut of AM parallel to build axis in the as-built condition
AM-Z	Z-cut of AM perpendicular to build axis in the as built condition
AM-HT1	AM after heat treatment for 24 h at 1200 °C
AM-HT2	AM after heat treatment for 200 h at 1100 °C
AM-HR	AM after hot rolling at 980 °C
AM-CG	AM after annealing for 100 h at 1250 °C to obtain coarse-grained structure
CM IN625	Conventional forged INCONEL 625

employed for grazing incidence X-ray diffraction (GI-XRD). A grazing incidence angle of 0.5–2° was used and a 2θ range of 20° – 90° was measured with a step size of 0.05°.

Electron backscatter diffraction (EBSD) maps were obtained on as-received materials using a Zeiss Ultra 55 field emission gun (FEG) scanning electron microscope (SEM) equipped with an HKL Channel 5 EBSD detector. An FEI Quanta 200 SEM equipped with an Oxford X-max 80 energy dispersive X-ray spectrometer (EDS) was employed for pre- and post-exposure analysis. Aztec software was used to evaluate the EDS data. Cross-sections were made on exposed samples by the broad-ion beam (BIB) technique using a Leica EM TIC 3X, as well as by conventional polishing with diamond pastes (0,25 μm) and colloidal silica (≈50 nm) after hot mounting into Bakelite. The surfaces of the samples prior to BIB were coated with gold by DC magnetron sputtering to enhance the contrast between the oxide and the insulating glue. Some specimens prepared by conventional metallographic polishing demonstrated poor oxide adherence and had to be electroplated with nickel to prevent the oxide scale from spalling during the sample preparation.

3. Results

3.1. Microstructure of as-built AM IN625

The microstructure obtained in AM IN625 after SLM is shown in Figs. 2 and 3. The EBSD inverse pole figure (IPF) maps in Fig. 3 show that non-equiaxed columnar grains were formed in AM IN625 as a result of rapid solidification. The elongated grains are aligned along the build axes with an average width of 30 μm (Fig. 3a). The grains in Z-cut are inclined at 45° as a result of the SLM process. Similar IN625 microstructures obtained by SLM were reported in [28]. The CM IN625 consists of equiaxed grains with the average grain size of 12 μm (Fig. 3c.).

Apart from the columnar grains in AM IN625, melt pool lines, another specific microstructural feature of the AM material, were present (Fig. 2a). They form along the build direction as a result of local re-melting and rapid-solidification of a previously deposited layer together with the new powder portion (Fig. 2a) [46–48].

Higher magnification SEM-SE images of AM IN625 (Fig. 2b and d) reveal a dendritic microstructure with an average dendrite spacing of 2.5 μm in both directions, in good agreement with literature [27]. Intermetallic precipitates were found along the dendritic boundaries for both Y and Z cuts, identified as δ-Ni_3Nb, which are typical for IN625 microstructure [12,13,27]. On the other hand, the AM variant of IN625 did not contain M_6C carbide common for CM IN625. The as-built AM IN625 was compact and did not contain any voids in the as-received microstructure.

Additionally, SEM-BSE images of heat treated (AM-HT1 (1200 °C, 24 h) and AM-HR are also illustrated in Fig. 2 while IPF maps corresponding to same materials were given in Fig. 3. After the heat treatment (AM-HT1), melt pool lines were no longer visible and the AM microstructure was replaced by a coarse-grained microstructure (Fig. 2e, Fig. 3d) typically observed in cast materials. The average grain size of this material is approximately 100 μm. Although not presented here, the AM IN625 heat treated at 1100 °C (AM-HT2) is composed of 60 μm sized grains, while the one heat treated at 1250 °C for 100 h (AM-CG) consisted of gigantic grains measuring mm in size. AM-HR (Fig. 2f, Fig. 3e) consisted of equiaxed grains with the average grain size of 15 μm, similar to CM IN625.

3.2. Oxidation behavior in air

Fig. 4 shows area specific weight change curves for AM and CM IN625 exposed in air at (a) 900 °C and (b) 1000 °C. The kinetic curves for both materials follow a parabolic rate law, the lines in Fig. 4 representing ideal parabolas. The anisotropy of the AM material does not affect oxidation kinetics, i.e., both Y- and Z-cuts show equal oxygen uptakes within the measurement errors. After 100 h at 1000 °C, mass loss due to oxide spalling on cooling was detected for the AM IN625 specimens. The latter is not surprising: reaching a critical oxide scale thickness 10 μm (1.7 mg/cm^2), 1–2 mm thick CM IN625 specimens are also prone to oxide spallation in air at 1000 °C [13].

The CM IN625 tested in the present study is the same bar from [13]. The oxidation kinetics data for the CM alloy were in good agreement with the previous measurements [13] as well as with available literature data [33,49–51] (Fig. 5). The oxidation kinetics of both AM and CM IN625 demonstrated high reproducibility at all temperatures and in all environments. Figs. 4 and 5 indicate faster oxidation kinetics of AM IN625 compared to CM IN625, while the trend increases with increasing temperature. Higher oxygen uptakes were previously reported for AM IN625 [33,36] and IN718 [34,35].

3.2.1. Oxide scale morphology in air

Fig. 6 shows top view SEM images of AM IN625-Z (a), AM IN625-Y (b) and CM IN625 (c) along with the corresponding EDS maps after 300 h in air at 900 °C. Both AM and CM alloys form protective external Cr_2O_3. Sporadic $NiCr_2O_4$ spinel protrusions were found on the surface of both materials. XRD analysis (not shown here) detected Cr_2O_3 (PDF 01–074–6677), $NiCr_2O_4$ spinel (PDF 00–023–1271) and rutile TiO_2 (PDF 04–003–0648) on the oxidized surface of the specimens. The main difference between AM IN625 and CM IN625 is the network of oxide ridges on all surfaces of the AM alloy. The ridges were decorated with Ti (Fig. 6).

Fig. 7 shows SEM-BSE overview images of the BIB cross-sectioned AM IN625 (a,b) and CM IN625-Z (c,d) after 168 h exposure at 900 °C. The oxidation morphology of the tested CM IN625 is in agreement with

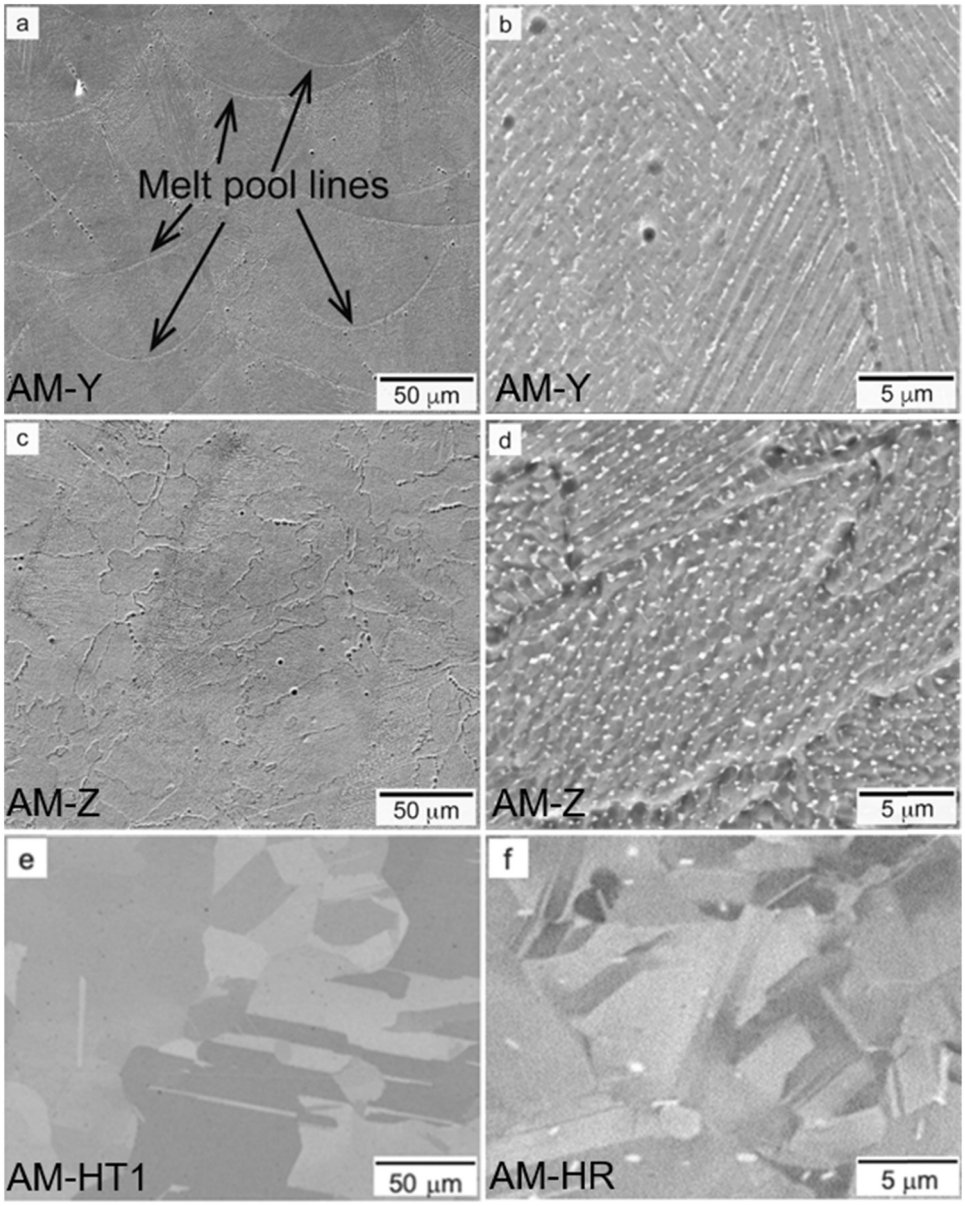

Fig. 2. SE images of AM IN 625, Y-cut (a,b) and Z-cut. (c,d), AM-HT1 (e), AM-HR (f).

the previously reported microstructural features [13–15,50]. The oxide scale is smooth, compact and consists of slightly undulating chromia followed by a subscale of intermetallic δ-Ni_3Nib and δ-depletion zone. The alloy grains in the δ-dissolution zone have coarsened and are bigger (15–20 μm) compared to those in the alloy bulk (7–12 μm). The alloy grain boundaries in the immediate vicinity of the oxide-alloy interface are decorated with internal Al_2O_3 precipitates. On the other hand, no complete δ-dissolution was observed in AM IN625. The δ-phase precipitates were found at the oxide-metal interface as well as at the GBs and in the voids that formed in the oxidation-affected zone (Fig. 7b). The studied batch of AM IN625 presumably contained slightly higher concentrations of Nb and/or Mo resulting in a δ-denuded zone rather than in δ-dissolution.

The smooth part of the chromia scale grown over an entire big grain of AM IN625 (see Fig. 7a) is equally thick to that on CM IN625 (3.5 μm) matching well the oxygen uptake by the latter (0.54 mg/cm^2). At the same time, the AM IN625 specimens took up 30–35% more oxygen after 300 h in air at 900 °C (0.75–0.80 mg/cm^2). The oxide scale grown on AM IN625 (Fig. 7a and b) revealed a number of different microstructural features suggesting the source of the excessive oxygen uptake. Oxide ridges observed in top-view SEM (Fig. 6) are located exactly over the grain boundaries (Fig. 7b). The ridges are accompanied by coarse elongated voids located at the respective grain boundaries. Such oxidation morphologies, hereafter termed as ridge-void (RV) associates, have been reported for AM IN625 [33,41] and AM 718 [34,35].

SEM BSE images and their corresponding-EDS maps of the BIB cross-sectioned AM IN625-Z, AM IN625-Y and CM IN625 after 168 h air exposure at 900 °C are displayed in Fig. 8. Both cuts show similar oxidation morphologies, showing that the oxide morphology is not affected by the microstructural anisotropy. The oxide scale thickness is also independent of cutting direction and was found to be approximately 3.5 μm. The ridges were thicker than the continuous scale by a factor of 2.0–2.5. Numerous submicron pores were detected in the chromia layer. Similar to CM IN625, a δ-Ni_3Nib layer formed underneath the chromia scale. The mechanism of the oxidation-induced δ-Ni_3Nib subscale precipitation was elaborated in [13]. In the Nb map of AM IN625-Z and AM IN625-Y (Fig. 8), the topmost layer corresponds to the gold layer deposited after the exposures and not to a Nb containing compound. The

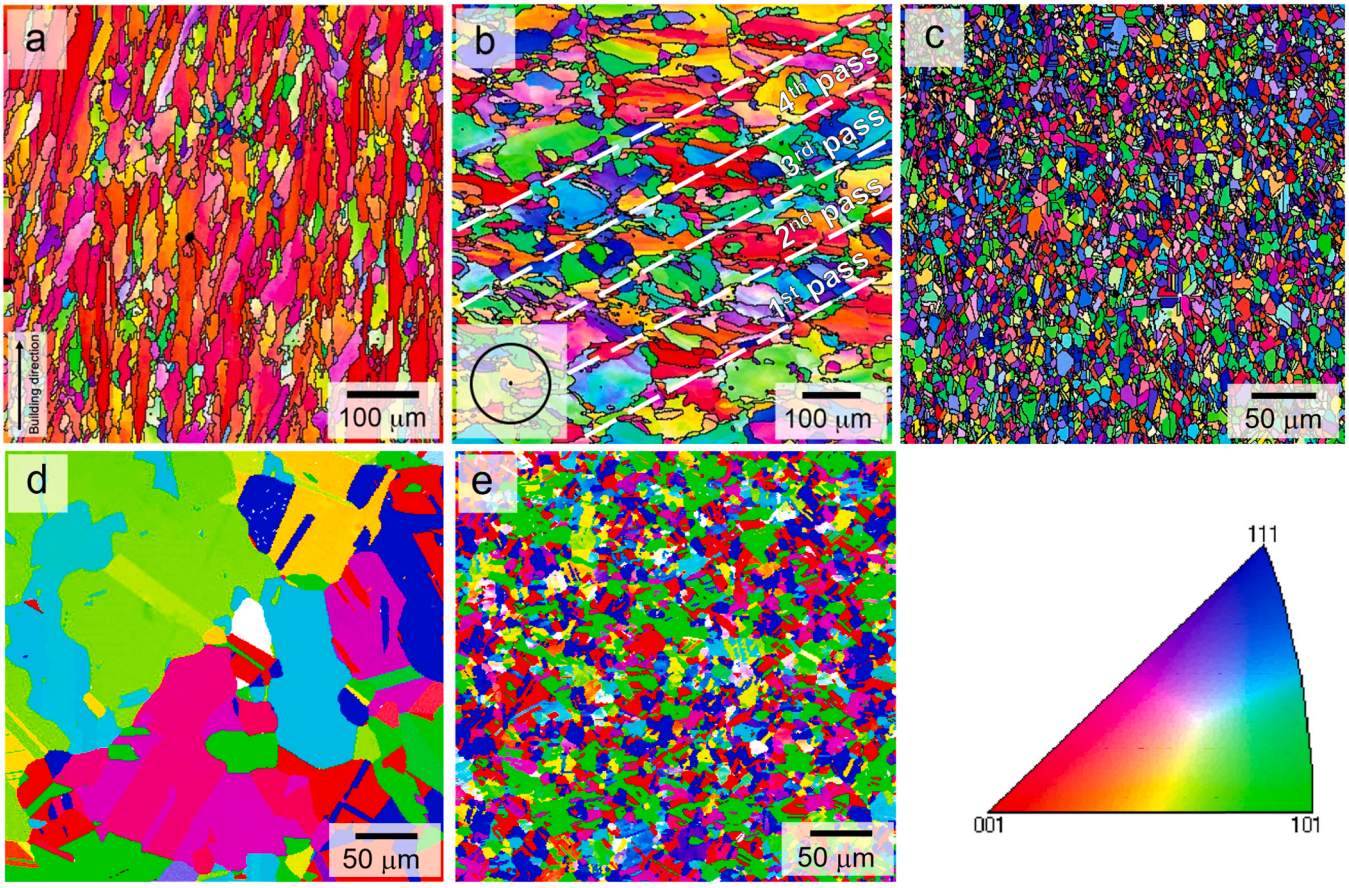

Fig. 3. Inverse pole figure maps of as-built AM-Y (a), AM-Z (b) and CM IN625 (c) AM-HT1 (d), AM-HR (e).

characteristic X-ray lines of Gold (M_α: 2.12 keV) and Nb (L_α: 2.166 keV) are close and often overlap in the EDX analysis. The Ti-rich precipitates observed in the oxide scale were attributed to TiO_2. Minor amounts of Al and O were detected at the grain boundaries of both AM and CM IN625 corresponding to internal oxidation of Al.

Fig. 9 presents a collage of BSE images demonstrating the dynamics of the oxide scale evolution on both cuts during early stages of air oxidation at 900 °C (a) and 1000 °C (b). Clearly, ridges and voids are correlated and appear already after 2 h of exposure. It is evident from the SEM images that the chromia is corrugated by the growth stress and buckles over the grain boundaries, resulting in the formation of voids below the buckled scale. Oxide delamination opens up the voids leading eventually to their oxidation. The latter is far more pronounced at 1000 °C (Fig. 9b): some voids are completely filled with oxide. After 100 h at 1000 °C, the oxide scale is smooth and uniform, and the ridges are overgrown. A horizontal crack can be observed in the oxide scale on the Z-cut specimen, suggesting approaching oxide spallation, in agreement with the thermogravimetric measurements (Fig. 4b).

Fig. 10 shows a schematic of an approximate oxygen uptake quantification method comprising four contributions: 1) m_{scale}, oxygen in smooth oxide scale; 2) m_{ridge}, oxygen in ridges; 3) m_{void}, oxide in voids, 4) $m_{alumina}$ oxygen tied-up by internal alumina. For the total oxygen uptake m_O^{total} is given thus by Eq. 1:

$$m_O^{total} = m_{scale} + m_{ridge} + m_{void} + m_{alumina} \quad (1)$$

Analysis of the SEM images suggests that m_{scale} can be reasonably equated to the oxygen uptake by CM IN625, since no ridges and voids are found in the oxide scale and in the zone beneath it, respectively. The oxide scale thickness over a grain is X_{ox}. Assuming the width and height of the oxide ridge, counting from the oxide-metal interface, being as $2X_{ox}$, the second term m_{ridge} can be roughly estimated as $2m_{scale}\frac{X_{ox}}{L_{GB}}$, here L_{GB} is the spacing between GBs, i.e. the grain size. Taking $X_{ox} = 5$ µm and $L_{GB} = 50$ µm, the ridge contribution can be estimates as approximately 20% for AM IN625. According to this approach, increasing the grain size to 100 µm (heat treatment) would diminish this contribution to 10% while decreasing it to 15 µm (hot rolling) would increase the excessive oxygen uptake to 40%. No such effect of grain size is observed during air oxidation of AM IN625. The overall excessive oxygen uptake amounts to 30–35% at 900 °C and even 100% at 1000 °C (Fig. 4). Obviously, oxidation of voids significantly contributes to the oxidation kinetics.

The contribution m_{void} can neither be directly measured nor reasonably estimated based on the pore volume since the extent of void oxidation is unknown. However, m_{void} can be estimated from the experimental value of m_O^{total} which is 30% higher than m_{scale} at 900 °C in air (Fig. 4a). Thus, the excessive oxygen uptake consists of two contributions: 2/3 in ridges and 1/3 in voids. The last term $m_{alumina}$ can be ignored due to low Al concentration in IN625.

3.3. Oxidation behavior in Ar-5%H_2-3%H_2O

It is well known that hydrogen/water atmospheres promote inward growth of chromia on chromia-forming alloys [13,52,53]. This inward grown chromia scales adhere better to the metal, preventing thus the oxide from delamination and oxidation of voids. Fig. 11 shows weight change curves for both cuts of AM IN625, CM IN625 and AM-HR in Ar-5%H_2-3%H_2O for up to 300 h at 900 °C. CM IN625 oxidizes faster in Ar-5%H_2-3%H_2O compared to air (Fig. 4a). Once again, the gravimetric measurements showed very good agreement with the previous data for Ar-4%H_2-4%H_2O at 900 °C reported in [13].

Conversely to air, in Ar-5%H_2-3%H_2O, AM IN625 revealed a clear dependence of oxidation kinetics to the microstructural anisotropy (Fig. 11). Having a higher grain boundary (GB) density on the surface,

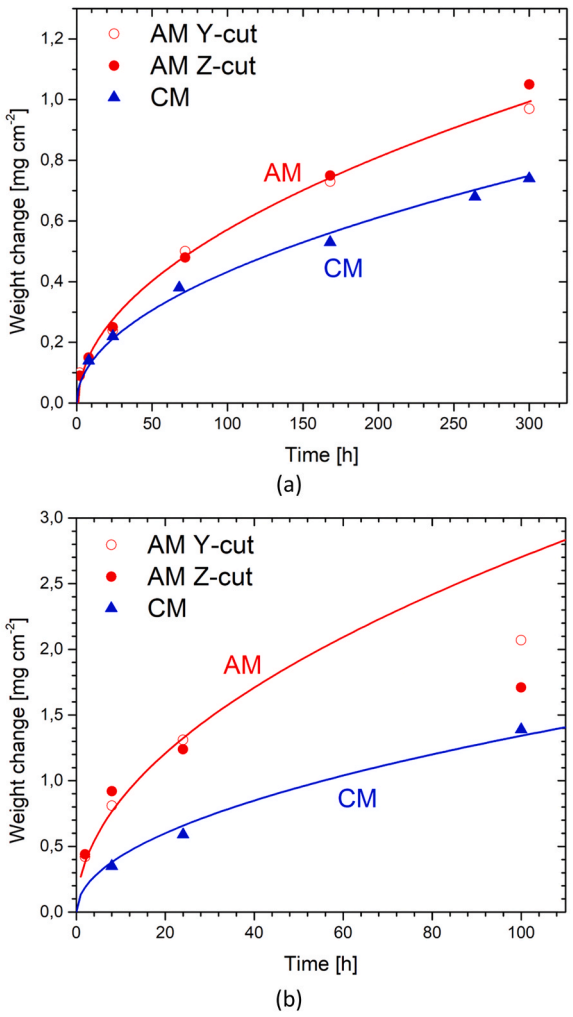

Fig. 4. Weight change curves for AM IN625 and CM IN625 in air at 900 °C (a) and 1000 °C (b). AM samples exhibited spallation at after 100 h at 1000 °C.

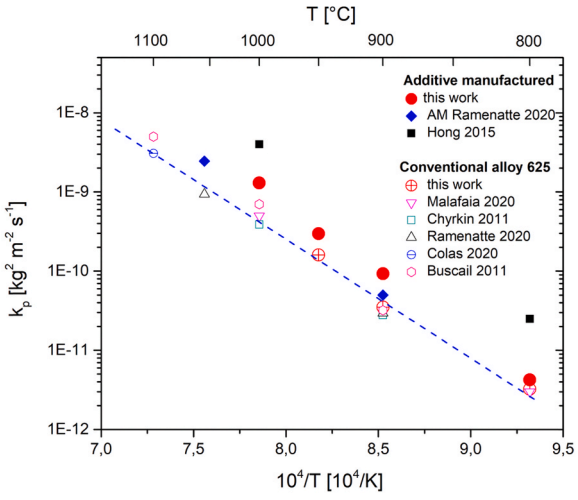

Fig. 5. Temperature dependence of parabolic rate constant for air oxidation of AM and CM IN 625: literature data and present study. The fit refers to all reported CM data.

the Z-cut specimens showed systematically higher oxygen uptake albeit the effect is not too strong (10% difference between Z-cut and Y-cut). More surprisingly, the difference between oxidation rates of AM IN625 and CM IN625 dramatically decreased in Ar-5%H_2-3%H_2O compared to that in air (see Fig. 4). In addition, AM-HR exhibited the fastest oxidation rate in Ar-5%H_2-3%H_2O.

Such a big difference in oxidation kinetics can be understood from electron microscopy. Fig. 12 shows the temporal evolution of the oxide scale morphology in Ar-5%H_2-3%H_2O for AM IN625 and the AM-HR IN625 variant. First of all, the chromia scale grown in Ar-5%H_2-3%H_2O is smoother, significantly more adherent and shows no signs of buckling and/or stress-induced delamination. Chromia scales are known to grow predominantly inward in H_2/H_2O and adhere much better to the metals. For example, the IN625 batch used in the present study showed no oxide spallation in Ar-4%H_2-4%H_2O for up to 1000 h at 1000 °C, oxide scales reaching 30 μm thickness), while in air chromia started spalling after 300 h at 1000 °C [13].

As the oxide scale doesn't buckle, the voids remain closed and intact. According to Eq. (1), the ridges contribute most to the excessive oxygen uptake. Oxidation in voids being eliminated, the excessive oxygen uptake reduces to m_{ridge} (note that ridges form in Ar-5%H_2-3%H_2O as well) and amounts to 10–15% for AM IN625, in good agreement with the approximative model (Eq. 1). If the oxidation kinetics in Ar-H_2-H_2O is thus dominated by the m_{ridge} contribution, the oxidation rate should increase with decreasing grain size. This trend is fully confirmed by the thermogravimetric data (Fig. 11); the oxidation rate increases as follows for the alloy with the same chemical composition: AM-Y (10%), AM-Z (20%), AM-HR (30%). The elimination of m_{void} from Eq. (1) thus allowed deconvoluting quantitively the excessive oxygen uptake contributions. Fig. 13 shows the SEM-EDS maps of AM-Z and AM-Y exposed in Ar-5%H_2-3%H_2O for 300 h at 900 °C. The elemental distribution patterns were very similar to those of the air exposed specimens (see Fig. 8).

3.4. *Effect of grain size*

Fig. 14 shows a comparison of the weight change curves for AM IN625, hot rolled AM IN625 (AM-HR), CM IN625 and homogenized AM IN625 with highly coarsened grains exposed in air for up to 300 h at 900 °C. Hot rolling, which resulted in a fine-grained alloy (AM-HR) microstructure similar to that of CM IN625, did not appreciably affect the oxidation rate. However, the heat treatment at 1250 °C resulting in gigantic grains of a few mm in size, virtually bi-crystals, lead to a significant drop of the oxidation kinetics below that of CM IN625 (Fig. 14). Fig. 15 illustrates the temporal evolution of the oxide scale morphology in air for AM-HR IN625. The SEM-BSE images in Fig. 15 demonstrate the typical ridge-void (RV) oxide scale morphologies of AM IN625 (Figs. 7–10). The ridges are more frequent in the AM-HR as the GB density after hot rolling is significantly higher compared to AM IN625. The other extreme in this system, which is illustrated in Fig. 16, is the alloy with gigantic grains (AM-CG) that revealed no ridges in the oxide scale. This finding clearly corroborates the main working hypothesis: the RV associates appear exclusively at GBs. In the exposed AM IN625 "bi-crystals", only one GB was found for per cross-section. Fig. 17 demonstrates such GBs facing the oxidized specimen surfaces. It is evident that the oxidation morphology over these GBs is that of the RV type.

Finally, moderately heat treated AM IN625 specimens to obtain acicular grains 60–100 μm (AM-HT1 and AM-HT2) in size revealed neither higher oxidation rates (oxygen uptakes comparable with those on both cuts of the as-built AM IN625) nor any different oxidation morphology. Both specimens pre-annealed at 1100 °C or 1200 °C developed RV associates at the GBs after 168 h of post-exposure in air at

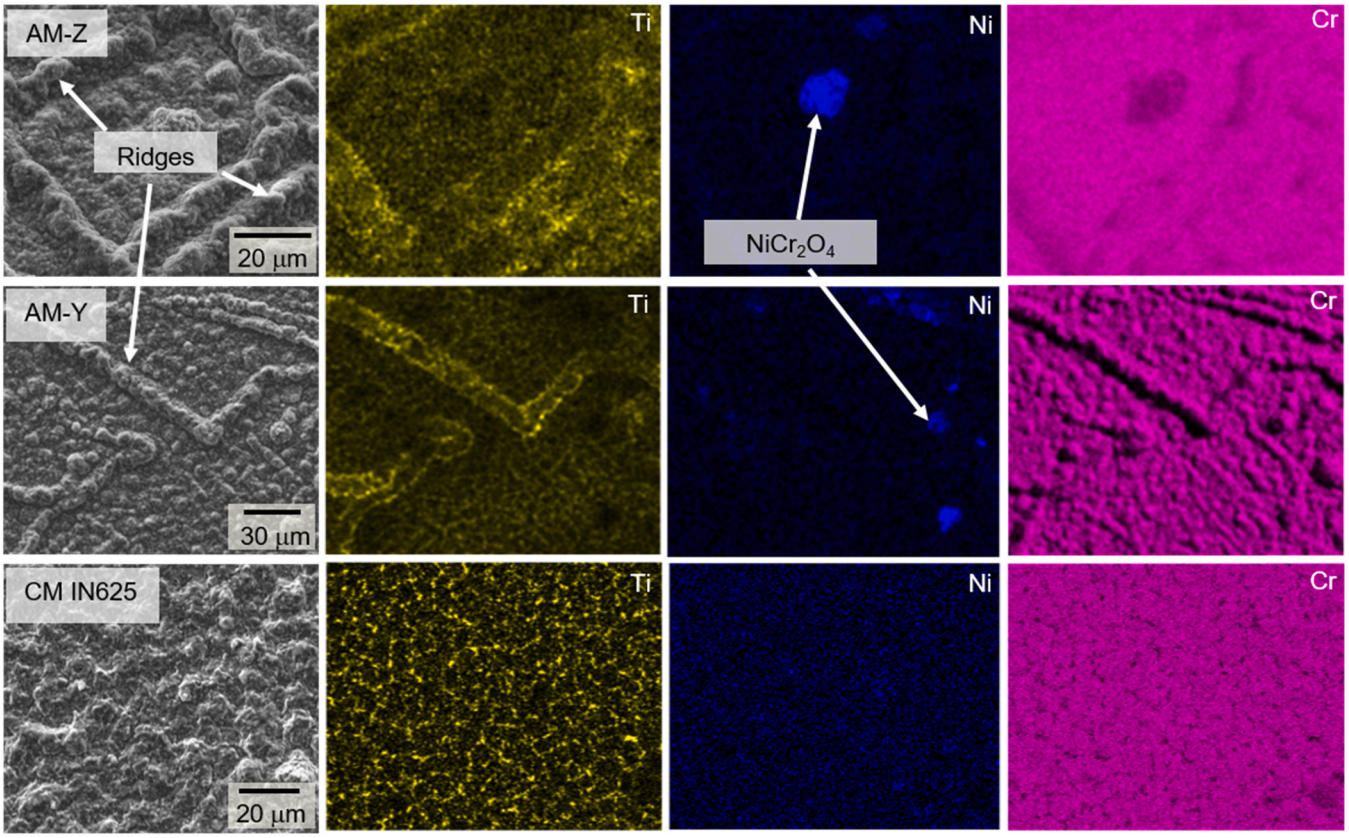

Fig. 6. SEM plan view images as well as EDS maps of AM-Z (a), AM-Y (b) and CM IN625 (c) after exposures for 168 h in air at 900 °C.

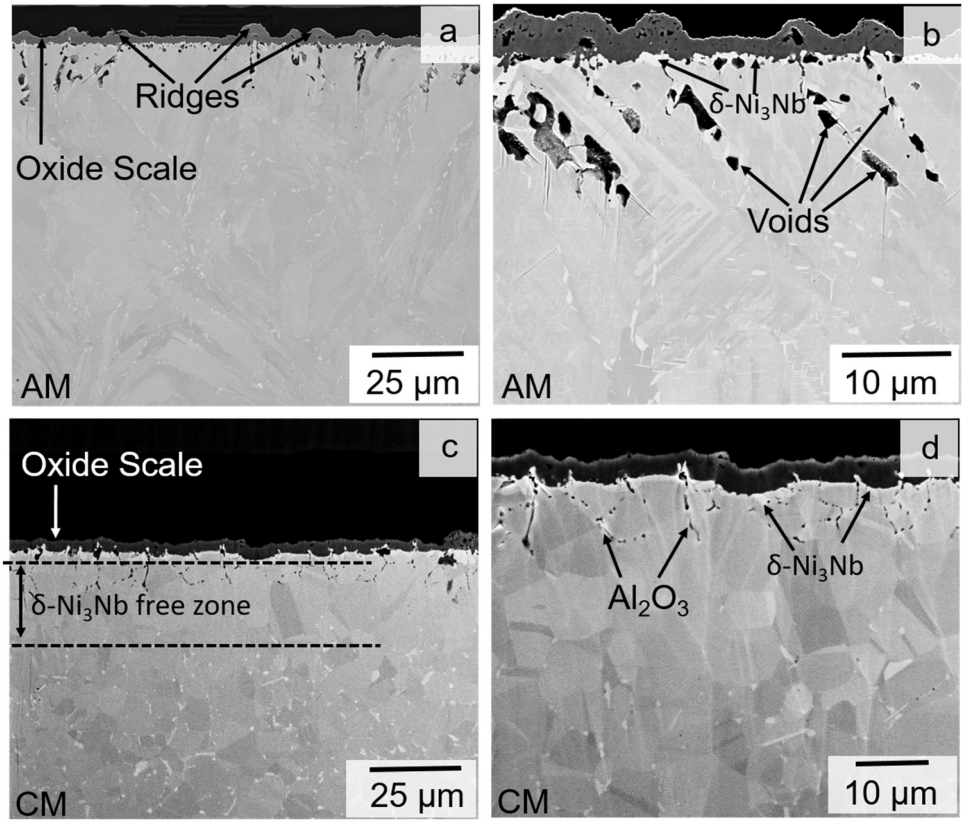

Fig. 7. Comparison of oxide scale morphologies after 168 h oxidation in lab air at 900 °C: AM IN625 (a,b) and CM IN625 (c,d).

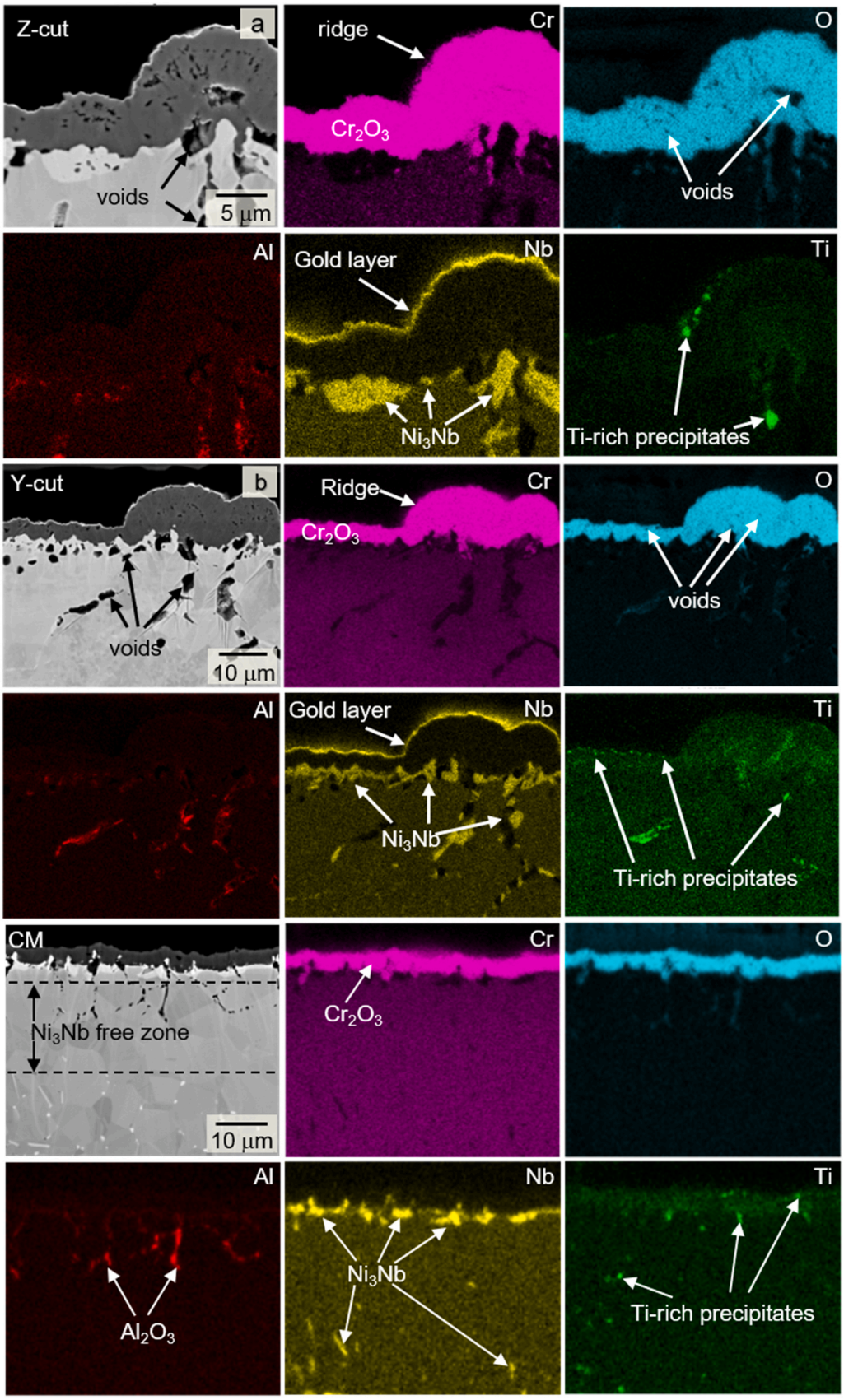

Fig. 8. SEM micrographs and EDS maps on BIB cross-sections of AM-Z (a), AM-Y (b) and CM IN625 (c) after air exposure for 168 h at 900 °C. Note the different magnifications.

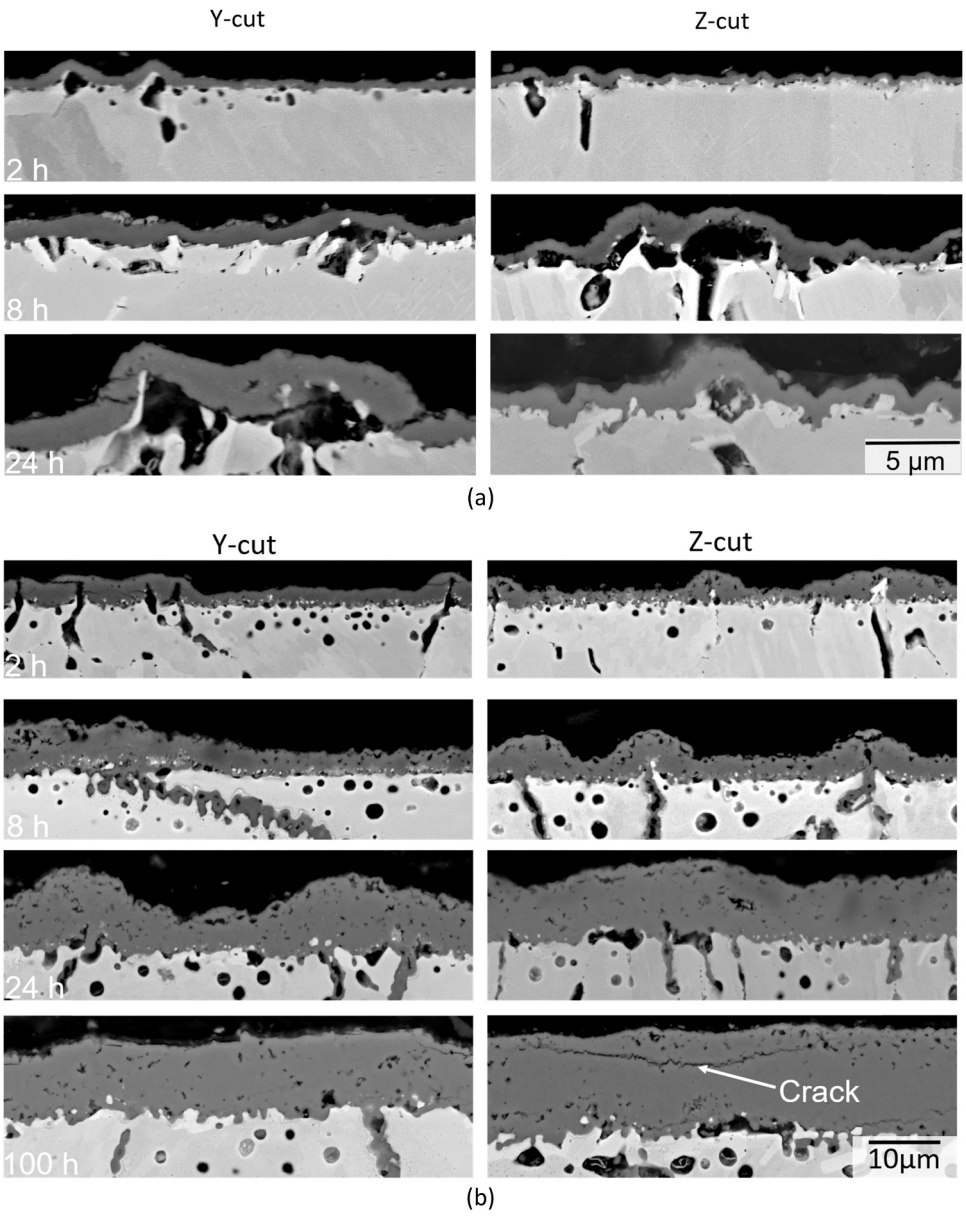

Fig. 9. SEM images of the temporal evolution of the oxide scales on AM IN625 during air oxidation at 900 °C (a) and 1000 °C (b).

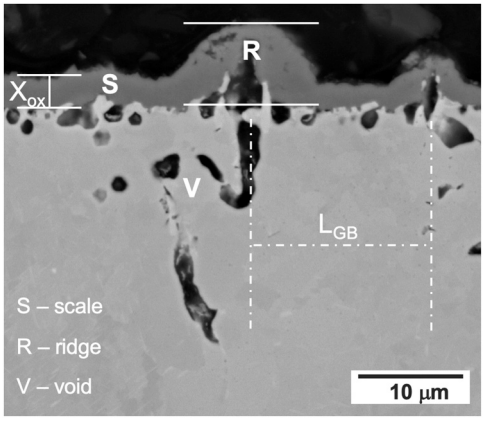

Fig. 10. Schematic of oxygen uptake quantification.

900 °C (Fig. 18). It is evident that the RV morphology is not a specific feature of the AM microstructure and is not affected by grain size, although its contribution becomes more pronounced with smaller grain size.

4. Discussion

4.1. Oxide ridges

Faster high-temperature oxidation of AM Ni-base alloys, mainly due to internal and intergranular oxidation, is a well-documented experimental fact [32–35,37,54]. The biggest difficulty in interpreting this observation is an obvious dilemma: are these differences caused by the AM microstructure or rather minor changes in alloy chemistry adopted to facilitate the AM process? To the best knowledge of the authors, this question remains to be solved up to this date. The goal of this study was to analyze the role of the microstructure on the oxidation behavior of AM IN625, i.e., kinetics, formation of RV associates, intergranular oxidation, etc. The AM microstructure was modified via hot rolling and

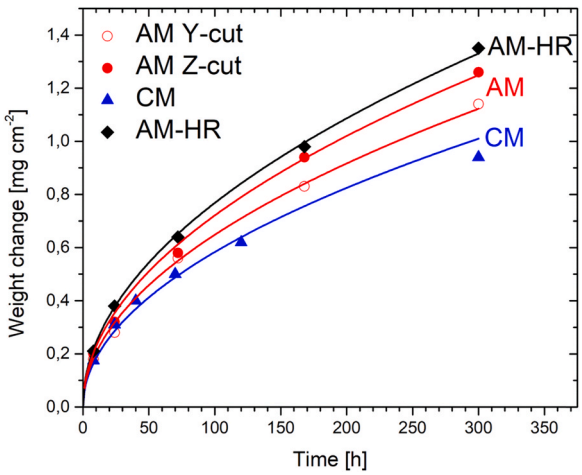

Fig. 11. Weight change curves for additively manufactured IN 625 (AM), AM-HR (hot-rolled AM) and CM IN625 exposed in Ar-5%H_2-3%H_2O for up to 300 h at 900 °C.

various heat treatments, while the chemical composition remained the same.

The main highlight of the present study is the RV associate forming at GBs facing the oxidized surface (Figs. 7–10), which is never observed for CM IN625 [13,15,50] (see also Fig. 7d), however, recurring in all possible conditions such as change of temperature (Fig. 9b), change of atmosphere for H_2/H_2O instead of air (Fig. 12a), hot rolling (Figs. 12b and 15), grain coarsening (Fig. 18) and severe heat treatment to obtain one single GB per specimen (Fig. 17). Thus, the RV associate formation is a specific feature of this AM IN625 alloy batch under investigation and presumably, is related to alloy chemical composition.

Parizia et al. [41] observed oxide buckling, as well as RV associates, at alloy GBs forming in the oxide scale on IN625 produced by laser powder bed fusion (LPBF) method after 96 h of air oxidation at 900 °C. Ramenatte et al. [33] observed moderate oxidation of subsurface voids in laser beam melted (LBM) IN625 at 1050 °C but not at 900 °C. However, the AM variant oxidized systematically faster than CM IN625, especially at 1050 °C. More commonly, the RV morphologies were reported for AM IN718 fabricated by SLM [37,55], EBM and LBM [34,35] and even for wrought IN718 [34] and alloy 690 [56].

Oxide thickenings above GBs in the form of outward ridges and/or inward grooves were often reported in literature for Ni-30Cr [57,58], AM IN718 [37], FeCrAl after wedge grinding of the oxide scale [59] and even pure nickel [60]. This phenomenon is commonly discussed in terms

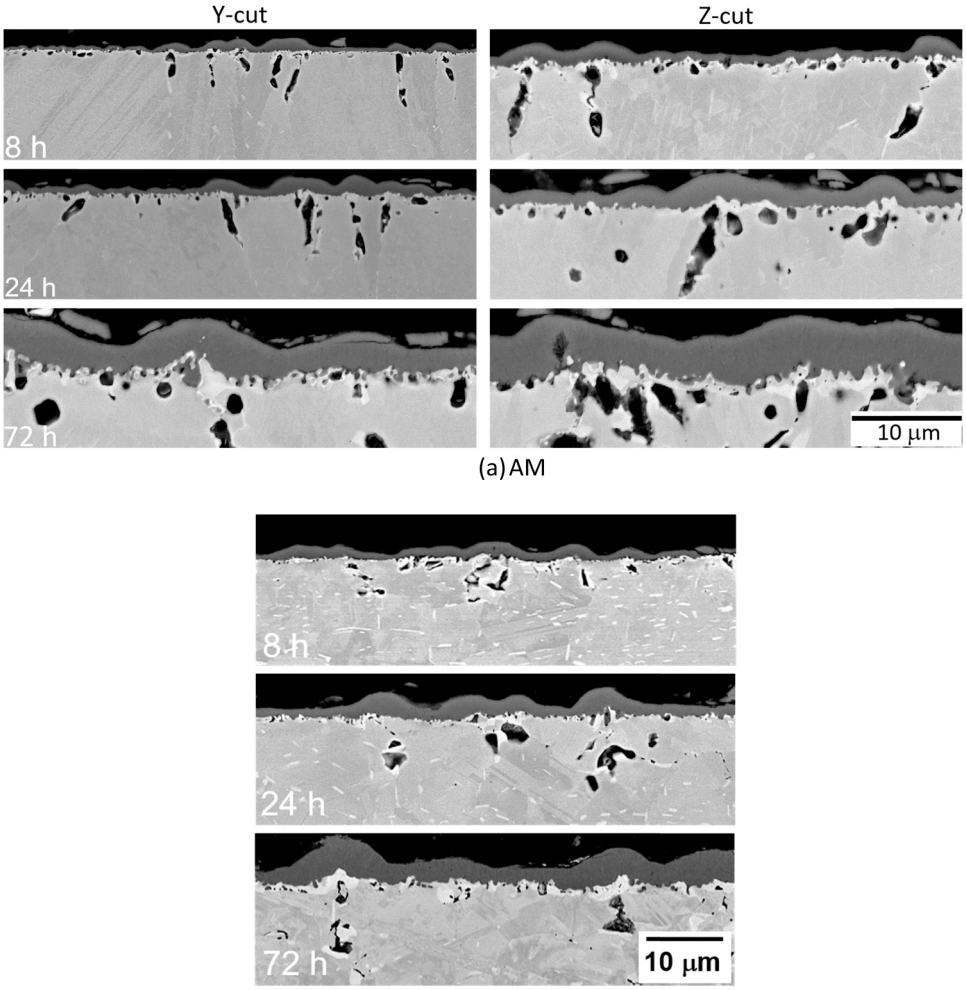

Fig. 12. Temporal evolution of oxide scales on AM IN625 during exposure in Ar-5%H_2-3%H_2O at 900 °C: SEM-BSE images of (a) AM IN625, (b) AM-HR (hot-rolled AM).

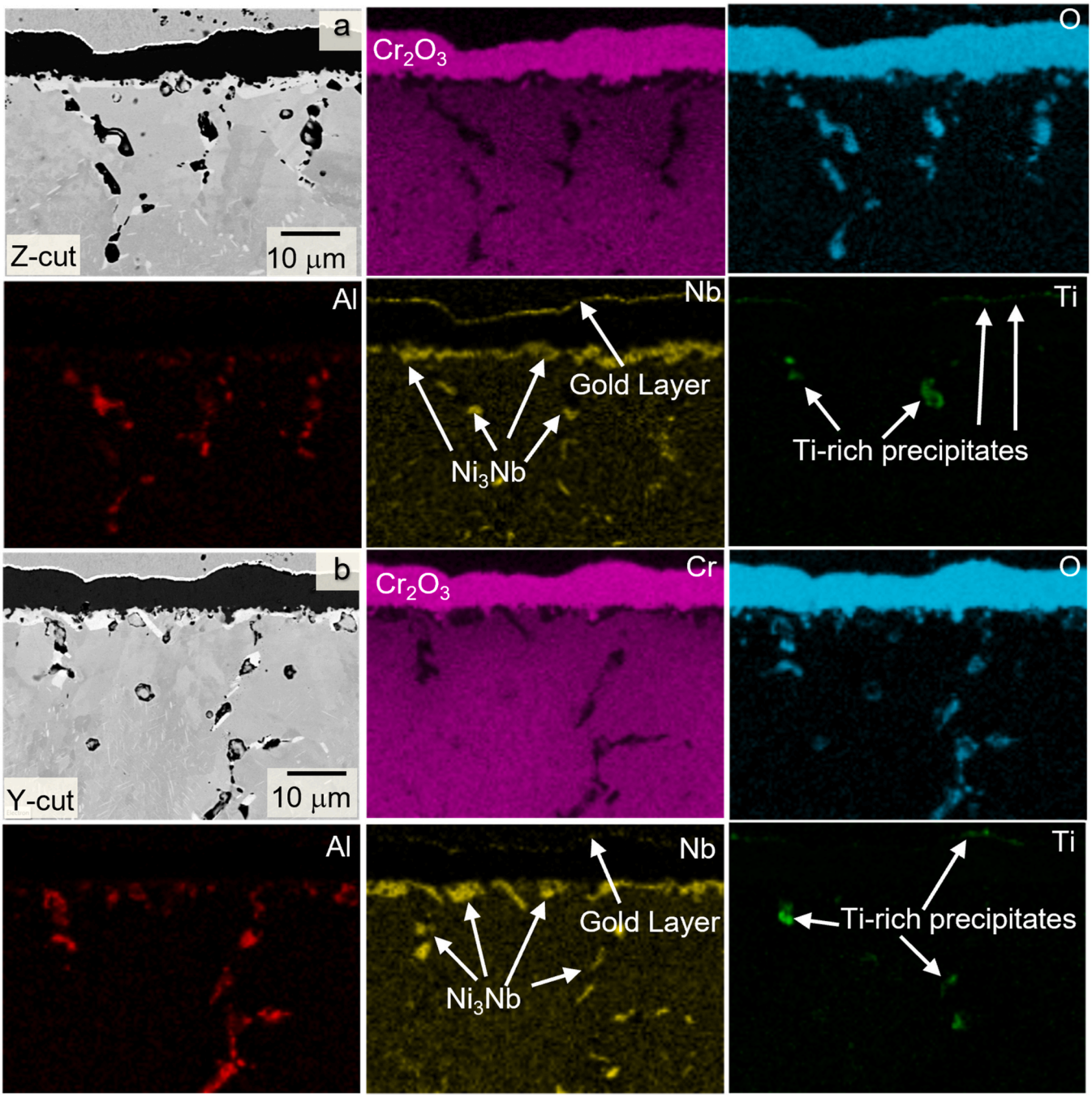

Fig. 13. SEM micrographs and EDS maps of BIB cross-sections of AM-Z (a), AM-Y (b) after Ar-5%H_2-3%H_2O exposure for 300 h at 900 °C.

of three main hypotheses: i) higher density of short-circuit paths in the oxide scale over alloy GB promoting the outward cation transport [57], ii) GBs serving as a very efficient vacancy sink [60] and iii) better supply of Cr over the GB. The latter interpretation appears the most plausible in the present case for two reasons. In Ar-5%H_2-3%H_2O, the outward cation diffusion is not the dominant scaling mode while the space created by injected vacancies is filled with inward growing chromia. Yet, the oxide ridges, albeit smoother ones, form in Ar-H_2-H_2O as well (Fig. 12). Even more convincing is the fact that the oxide scale formed on AM IN625 "bi-crystals" (Fig. 16) is twice as thin compared to that on as-built (Fig. 9a) and hot rolled AM IN625 (Fig. 15) and even thinner than that on CM IN625 (Fig. 14). Without grain boundaries in the microstructure, the chromia scale growth dramatically slows down (Fig. 13).

4.2. Voids

Voids often form in the surface-near region of chromia- and alumina-forming high-temperature alloys during oxidation. The principal void formation mechanisms such as vacancy injection [61] and the Kirkendall effect [62,63] are comprehensively reviewed in [64]. One should distinguish between interfacial voids [65,66], voids in the bulk and voids at grain boundaries [67]. All three types of voids were observed in AM IN625 (Figs. 7–10). The interfacial voids can be filled with inward growing oxide [65,66], which clearly takes place in Ar-5%H_2-3%H_2O (compare e.g. Figs. 12b and 15).

Bulk spherical voids become more abundant at higher temperatures, e.g. (Fig. 9), which was previously observed for IN625 [13,33]. Notably, bulk void formation can be exacerbated by higher Cr consumption [15,

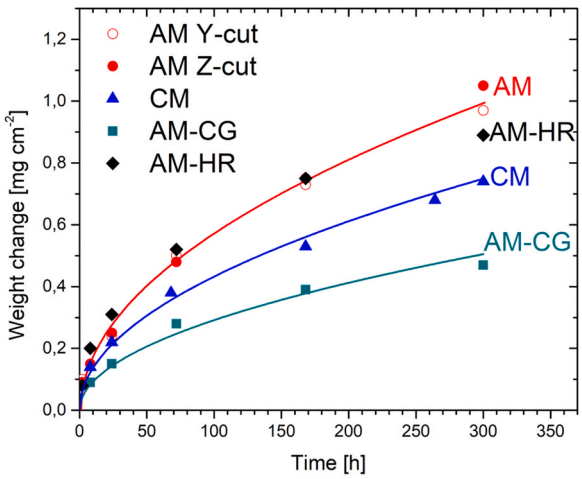

Fig. 14. Effect of grain size on oxidation kinetics of AM IN 625 in air at 900 °C: AM (as-built), CM (conventionally manufactured), AM-HR (hot rolled AM), AM-CG (coarse-grained AM).

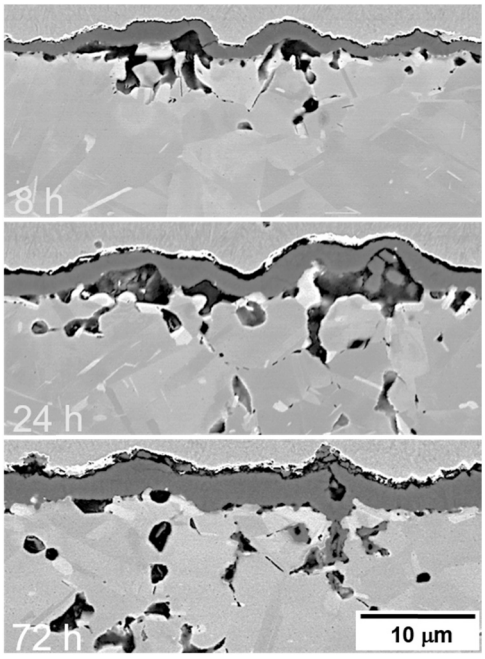

Fig. 15. SEM micrographs illustrating the temporal evolution of oxide scales on AM-HR during air oxidation at 900 °C.

68,69] due to reactive Cr-evaporation [70,71] or oxide spallation [72]. Bulk voids are susceptible to the Cr-depletion gradient in the surface near region or, in other words, to the k_p/D_{Cr} ratio. Hence, both mechanisms, vacancy injection (Cr consumption rate, k_p) and the Kirkendall effect (interdiffusion coefficient, D_{Cr}) are operative and can be affected by the experimental parameters such as temperature, gas composition and surface finish. Most importantly, the former Cr-consumption effect was responsive to the grain size modification. While virtually no bulk voids were found in the most fine-grained AM-HR (Fig. 12b, and 15), numerous spherical voids were detected in the moderately heat treated alloys AM HT1 and AM-HT2 (Fig. 18) and especially in "bi-crystals" (AM-CG) (Fig. 16). The latter is extremely remarkable since the oxygen uptakes, and thus Cr-removal rate, dropped by a factor of two after homogenization of AM IN625 at 1250 °C (Fig. 14) due to elimination of GBs. However, the GB-free microstructure resulted in also in slower Cr-diffusion and a steeper Cr-depletion profile.

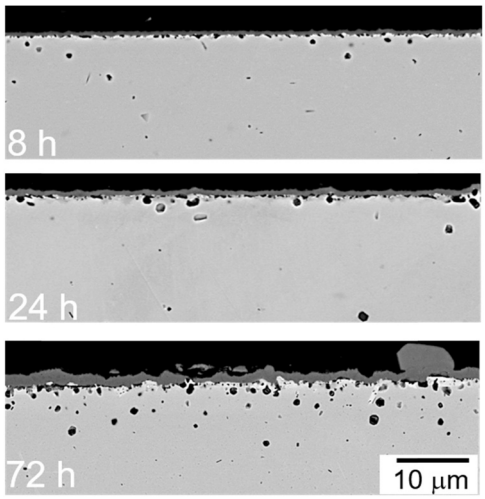

Fig. 16. SEM micrographs illustrating the temporal evolution of oxide scales on AM-CG (annealed for 100 h at 1250 °C) during air oxidation at 900 °C.

Finally, the elongated voids at GBs are present in all variants of AM IN625 but not in CM 625. Clearly, these voids are related to the chromia ridges above them. In the fine-grained hot rolled alloy variant the GB voids are not elongated but form a streak of spherical voids as a result of geometrical constraints (Figs. 12b and 15). Similar to the bulk voids, the GB voids originate from a faster local Cr-consumption by the accelerated growth of chromia ridges above them. Alternatively, Harris [73] argued that intergranular voids form and grow via creep under stresses imposed by a growing oxide scale. However, only thin-walled components prone to plastic deformation were discussed in [73], which is why this argumentation does not apply to the present results. Intergranular voids play a crucial role in oxidation kinetics of AM IN625 as their oxidation provide up to 1/3 of excessive oxygen uptake in air (see Eq. 1) and they pertain in all testing conditions.

4.3. *Microstructure or chemical composition*

The key question to answer in this study is why no RV associates appear in the chromia scale grown on CM IN625? The original AM microstructure resulting from recurring melting-solidification cycles during manufacturing can hardly be an explanation. The RV associates reappeared in the oxide scales after all heat treatment procedures which completely remove the AM microstructure (Figs. 16–18). Neither the fine-grained microstructure of CM IN625, and thus enhanced Cr transport to the surface, can be a satisfying explanation. The AM-HR IN625 developed RV associates in the oxidation morphology (Figs. 12 and 15) albeit the void pattern was different: no elongated voids at the GBs due to the smaller grain size.

It is evident that the RV associates originate from a complex and dynamic interplay of the solid-state transport phenomena: i) the oxide grows faster over the GBs, presumably due to a higher Cr supply through the GB; ii) enhanced Cr consumption over the GB leads to a local supersaturation of vacancies and their coalescence at the GB. Depending on the gas composition, the oxide scale may buckle and delaminate (air) or not (Ar-H_2-H_2O), thus accelerating the overall oxidation kinetics, i.e. excessive oxygen uptake (Figs. 4 and 11).

Since the RV mechanism is not susceptible to the alloy microstructure, the answer should be sought elsewhere, e.g., alloy chemical composition, GB chemistry and/or segregations at GBs. Minor alloying elements such as Ti, Mn, Si, Al, C and S may affect chromia growth as well as GB diffusion in the alloy. Titanium is known to accelerate chromia growth and have a deleterious effect on oxidation resistance of chromia-formers [74,75]. Manganese can form an external layer of $MnCr_2O_4$ over the chromia scale reducing thus Cr-evaporation [76].

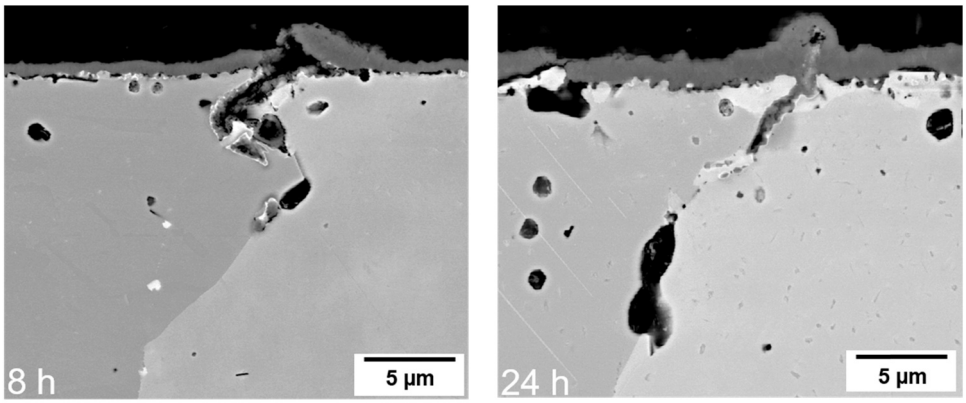

Fig. 17. SEM-BSE images of oxide scale above a grain boundary in AM-CG (heat treated for 100 h at 1250 °C) after (a) 8 h and (b)24 h air oxidation at 900 °C.

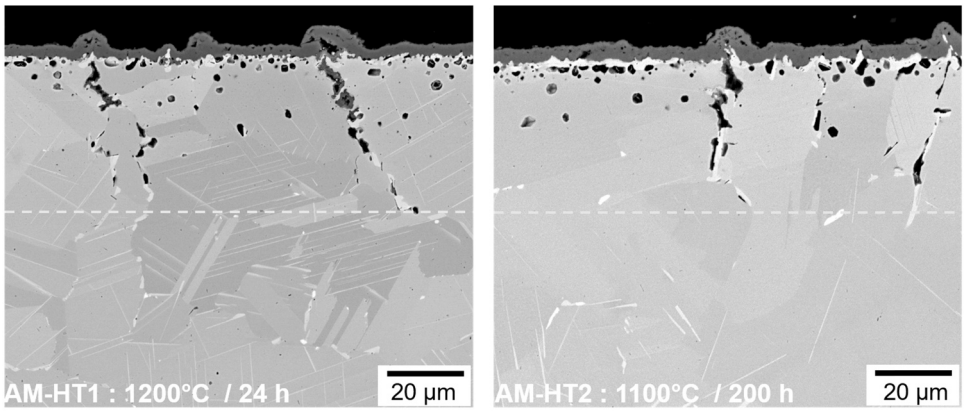

Fig. 18. BSE images of oxide scales on heat treated AM IN 625 after 168 h of air oxidation at 900 °C: (a) AM-HT1 (annealed for 24 h at 1200 °C) (b) AM-HT2: (annealed for 200 h at 1100 °C).

Silicon and aluminum [77] are prone to internal oxidation underneath the chromia scale, while the former can, in certain circumstances, form a SiO_2 subscale [78–81] partially blocking the Cr transport into the scale, thus reducing the overall oxide growth rate. Carbon along with other interstitial impurities, such as N, S, P, tend to segregate to the GBs and dramatically affect GB diffusion [82]: the purer the metal, faster the GB diffusion. Therefore, a thorough analysis of the minor differences in chemical composition between AM and CM IN625 is required to shed light on the role of alloy chemistry, fine-tuned to optimize the AM process, in the oxidation behavior of AM Ni-base alloys.

5. Conclusions

5.1. Oxidation kinetics

Additively manufactured (AM) Ni-base alloy Inconel 625 demonstrated faster oxidation kinetics (up to 30%) compared to its conventionally manufactured (CM) counterpart when exposed in lab air at 900–1000 °C.

- The faster growth kinetics is largely caused by oxide ridges growing over the alloy grain boundaries (GB) as well as intergranular oxidation of the voids forming immediately underneath the ridges.
- A clear morphological pattern was established: oxide ridges form above GBs correlating with an elongated void in the alloy subsurface in the immediate vicinity of the oxide-metal interface. Oxide buckling and delamination is shown to induce oxidation of the voids.
- Oxidation kinetics of AM IN625 has three main contributions: i) chromia oxide scale over the grain, ii) oxide in the ridge over the GB, iii) oxides in the void.
- Exposures in Ar-H_2-H_2O suppressed oxide delamination and, hence, oxidation of the voids at the GBs (contribution iii) significantly diminished the discrepancy between the AM and CM oxidation rates. However, AM IN625 still oxidized faster due to the ridge contribution.
- As long as all three oxidation contributions are active, e.g., during air oxidation, no detectable effect of the AM microstructure, specifically the anisotropy and GB density, on oxidation kinetics is observed. In Ar-H_2-H_2O, the Z-cut specimens, the ones with the highest GB density, systematically oxidized faster than the Y-cuts due to the larger ridge contribution.

5.2. AM microstructure

Manipulations with the AM microstructure such as various heat treatments and hot rolling were shown to affect the overall oxidation kinetics to some extent. However, the principal oxidation morphology was grain size independent. The ridge-void (RV) associate over the GB appeared in the oxide scale structure after all microstructural treatments.

- Hot rolling of AM IN625, resulting in a fine-grained microstructure, did not affect the oxidation kinetics in air while accelerated it in Ar-H_2-H_2O due to a thicker GB network and a larger ridge contribution to the oxidation kinetics.
- Moderate heat treatments to coarsen the grains up to 100 μm neither changed the oxidation rate nor the oxide scale morphology. The characteristic RV associate formation was not affected by heat treatment.
- An ultrahigh-temperature homogenization at 1250 °C resulting in grains coarsened to a few mm in size revealed significantly lower oxidation kinetics, even lower than that of CM highlighting thus the crucial role of GBs in the oxidation/Cr supply dynamics.

Accelerated oxidation kinetics of AM Inconel 625 resulting from the additional oxidation contributions, such as ridge growth and oxidation of the void underneath, does not originate from the characteristic AM microstructure, specifically, grain size. Minor differences in alloy chemistry are thus more likely to be responsible for this oxidation behavior of the AM material compared to CM.

CRediT authorship contribution statement

Anton Chyrkin: Conceptualization, Investigation, Writing – original draft, Writing – review & editing, **Kerem O. Gunduz:** Investigation, Writing – original draft, Writing – review & editing, **Irina Fedorova:** Investigation, Writing – review & editing, **Mohammad Sattari:** Investigation, **Alberto Visibile:** Investigation, Writing – review & editing, **Mats Halvarsson:** Writing – review & editing, Funding acquisition, Project administration, **Jan Froitzheim:** Writing – review & editing, Funding acquisition, Project administration **Krystyna Stiller:** Writing – original draft, Writing – review & editing.

Declaration of Competing Interest

The authors declare that they have no known competing financial interests or personal relationships that could have appeared to influence the work reported in this paper.

Data Availability

The raw/processed data required to reproduce these findings will be made available on request.

Acknowledgements

This study was accomplished within the Swedish High Temperature Corrosion Centre (HTC) and thus the authors gratefully acknowledge HTC together with the Swedish Energy Agency and its Member Companies (Siemens Energy AB, AB Sandvik Materials Technology, Kanthal AB). The authors also gratefully acknowledge Chalmers Materials Analysis Laboratory (CMAL) where characterizations were carried out. Dr. D. Naumenko from Forschunszentrum Jülich GmbH, Jülich, Germany is kindly acknowledged for providing CM IN625.

References

[1] D. Young, High Temperature Oxidation and Corrosion of Metals, second ed., Elsevier Corrosion Series, 2016.
[2] B. Gorr, S. Schellert, F. Müller, H.-J. Christ, A. Kauffmann, M. Heilmaier, Current status of research on the oxidation behavior of refractory high entropy alloys, Adv. Eng. Mater. 23 (2021), 2001047, https://doi.org/10.1002/adem.202001047.
[3] B.R. Anne, S. Shaik, M. Tanaka, A. Basu, A crucial review on recent updates of oxidation behavior in high entropy alloys, SN Appl. Sci. 3 (2021) 366, https://doi.org/10.1007/s42452-021-04374-1.
[4] S.P. Hagen, M. Weiser, D. Kubacka, E. Spiecker, S. Virtanen, On the high-temperature oxidation behavior of a Ta-containing quaternary Co-base model alloy system with γ/γ′-microstructure - influence of γ′-volume fraction, surface state, and heating condition on alumina growth, Oxid. Metals 94 (2020) 477–503, https://doi.org/10.1007/s11085-020-10003-w.
[5] C.H. Zenk, S. Neumeier, N.M. Engl, S.G. Fries, O. Dolotko, M. Weiser, S. Virtanen, M. Göken, Intermediate Co/Ni-base model superalloys — Thermophysical properties, creep and oxidation, Scripta Materialia 112 (2016) 83–86, https://doi.org/10.1016/j.scriptamat.2015.09.018.
[6] M.P. Brady, Y. Yamamoto, M.L. Santella, P.J. Maziasz, B.A. Pint, C.T. Liu, Z.P. Lu, H. Bei, The development of alumina-forming austenitic stainless steels for high-temperature structural use, JOM 60 (2008) 12, https://doi.org/10.1007/s11837-008-0083-2.
[7] B. Gleeson, High-temperature corrosion of metallic alloys and coatings, Mater. Sci. Technol. A Compreh. Treat. (2000) 173–228, https://doi.org/10.1002/9783527619306.ch14.
[8] H.L. Eiselstein, D.J. Tillack, The invention and definition of alloy 625, in: E.A. Loria (Ed.), Superalloys 718, 625 and Various Derivatives, The Minerals, Metals & Materials Society, 1991: pp. 1–14. https://doi.org/10.7449/1991/superalloys_1991_1_14.
[9] M.D. Mathew, K. Bhanu Sankara Rao, S.L. Mannan, Creep properties of service-exposed Alloy 625 after re-solution annealing treatment, Mater. Sci. Eng. A 372 (2004) 327–333, https://doi.org/10.1016/j.msea.2004.01.042.
[10] M.D. Mathew, P. Parameswaran, K.B.S. Rao, Microstructural changes in alloy 625 during high temperature creep, Mater. Charact. 59 (2008) 508–513.
[11] S. Patel , J. deBarbadillo , S. Coryell , E. Ott , X. Liu , J. Andersson , Z. Bi , K. Bockenstedt , I. Dempster , J. Groh , K. Heck , P. Jablonski , M. Kaplan , D. Nagahama , C. Sudbrack , Superalloy 718: Evolution of the Alloy from High to Low Temperature Application BT - Proceedings of the 9th International Symposium on Superalloy 718 & Derivatives: Energy, Aerospace, and Industrial Applications 2018 Springer International Publishing Cham 23 49.
[12] M. Sundararaman, P. Mukhopadhyay, S. Banerjee, Precipitation of the δ-Ni3Nb phase in two nickel base superalloys, Metall. Trans. A 19 (1988) 453–465, https://doi.org/10.1007/BF02649259.
[13] A. Chyrkin, P. Huczkowski, V. Shemet, L. Singheiser, W.J. Quadakkers, Sub-scale depletion and enrichment processes during high temperature oxidation of the nickel base alloy 625 in the temperature range 900-1000 °c, Oxidation Metals 75 (2011) 143–166, https://doi.org/10.1007/s11085-010-9225-3.
[14] L. García Fresnillo, A. Chyrkin, T. Hüttel, C. Böhme, J. Barnikel, D. Grüner, F. Schmitz, W.J. Quadakkers, Oxide scale formation and subsurface phase transformations during long-term steam exposure of the cobalt base alloy 25, Mater. Corr. 63 (2012) 878–888, https://doi.org/10.1002/maco.201206683.
[15] P. Huczkowski, W. Lehnert, H.H. Angermann, A. Chyrkin, R. Pillai, D. Grüner, E. Hejrani, W.J. Quadakkers, Effect of gas flow rate on oxidation behaviour of alloy 625 in wet air in the temperature range 900–1000 °C, Mater. Corr. 68 (2017) 159–170, https://doi.org/10.1002/maco.201608831.
[16] T. DebRoy, H.L. Wei, J.S. Zuback, T. Mukherjee, J.W. Elmer, J.O. Milewski, A. M. Beese, A. Wilson-Heid, A. De, W. Zhang, Additive manufacturing of metallic components – process, structure and properties, Prog. Mater. Sci. 92 (2018) 112–224, https://doi.org/10.1016/j.pmatsci.2017.10.001.
[17] K.V. Wong, A. Hernandez, A review of additive manufacturing, ISRN Mech. Eng. 2012 (2012), 208760, https://doi.org/10.5402/2012/208760.
[18] W.E. Frazier, Metal additive manufacturing: a review, J. Mater. Eng. Perform. 23 (2014) 1917–1928, https://doi.org/10.1007/s11665-014-0958-z.
[19] B. Anush Raj, J.T. Winowlin Jappes, M. Adam Khan, V. Dillibabu, N.C. Brintha, Direct metal laser sintered (DMLS) process to develop Inconel 718 alloy for turbine engine components, Optik 202 (2020), 163735, https://doi.org/10.1016/j.ijleo.2019.163735.
[20] C.Y. Yap, C.K. Chua, Z.L. Dong, Z.H. Liu, D.Q. Zhang, L.E. Loh, S.L. Sing, Review of selective laser melting: materials and applications, Appl. Physics Rev. 2 (2015) 41101, https://doi.org/10.1063/1.4935926.
[21] P.K. Gokuldoss, S. Kolla, J. Eckert, Additive manufacturing processes: selective laser melting, electron beam melting and binder jetting—selection guidelines, Materials 10 (2017), https://doi.org/10.3390/ma10060672.
[22] A. Sola, A. Nouri, Microstructural porosity in additive manufacturing: the formation and detection of pores in metal parts fabricated by powder bed fusion, J. Adv. Manuf. Process. 1 (2019), e10021, https://doi.org/10.1002/amp2.10021.
[23] A.B. Spierings, G.N. Levy, Comparison of density of stainless steel 316 L parts produced with selective laser melting using different powder grades, in: 2009.
[24] L.E. Murr, E. Martinez, S.M. Gaytan, D.A. Ramirez, B.I. Machado, P.W. Shindo, J. L. Martinez, F. Medina, J. Wooten, D. Ciscel, U. Ackelid, R.B. Wicker, Microstructural architecture, microstructures, and mechanical properties for a nickel-base superalloy fabricated by electron beam melting, Metall. Mater. Trans. A 42 (2011) 3491–3508, https://doi.org/10.1007/s11661-011-0748-2.
[25] G.P. Dinda, A.K. Dasgupta, J. Mazumder, Laser aided direct metal deposition of inconel 625 superalloy: microstructural evolution and thermal stability, Mater. Sci. Eng. A 509 (2009) 98–104, https://doi.org/10.1016/j.msea.2009.01.009.
[26] F. Zhang, L.E. Levine, A.J. Allen, C.E. Campbell, E.A. Lass, S. Cheruvathur, M. R. Stoudt, M.E. Williams, Y. Idell, Homogenization kinetics of a nickel-based superalloy produced by powder bed fusion laser sintering, Scripta Materialia 131 (2017) 98–102, https://doi.org/10.1016/j.scriptamat.2016.12.037.
[27] E.A. Lass, M.R. Stoudt, M.E. Williams, M.B. Katz, L.E. Levine, T.Q. Phan, T. H. Gnaeupel-Herold, D.S. Ng, Formation of the Ni3Nb δ-phase in stress-relieved inconel 625 produced via laser powder-bed fusion additive manufacturing, Metall. Mater. Trans. A 48 (2017) 5547–5558, https://doi.org/10.1007/s11661-017-4304-6.
[28] A. Kreitcberg, V. Brailovski, S. Turenne, Effect of heat treatment and hot isostatic pressing on the microstructure and mechanical properties of Inconel 625 alloy processed by laser powder bed fusion, Mater. Sci. Eng. A 689 (2017) 1–10, https://doi.org/10.1016/j.msea.2017.02.038.

[29] K. Gola, B. Dubiel, I. Kalemba-Rec, Microstructural changes in inconel 625 alloy fabricated by laser-based powder bed fusion process and subjected to high-temperature annealing, J. Mater. Eng. and Perform. 29 (2020) 1528–1534, https://doi.org/10.1007/s11665-020-04605-3.

[30] J. Dutkiewicz, Ł. Rogal, D. Kalita, K. Berent, B. Antoszewski, H. Danielewski, M. St. Węglowski, M. Łazińska, T. Durejko, T. Czujko, Microstructure and properties of inconel 625 fabricated using two types of laser metal deposition methods, Materials 13 (2020) 1–17, https://doi.org/10.3390/ma13215050.

[31] G. Marchese, A. Aversa, E. Bassini, Microstructure and hardness evolution of solution annealed inconel 625/tic composite processed by laser powder bed fusion, Metals 11 (2021), https://doi.org/10.3390/met11060929.

[32] S. Dryepondt, M.M. Kirka, F.A. List III, Oxidation Behavior of Ni-Based Alloys Fabricated by Additive Manufacturing, in: 2019.

[33] N. Ramenatte, A. Vernouillet, S. Mathieu, A. Vande Put, M. Vilasi, D. Monceau, A comparison of the high-temperature oxidation behaviour of conventional wrought and laser beam melted Inconel 625, Corros. Sci. 164 (2020), https://doi.org/10.1016/j.corsci.2019.108347.

[34] T. Sanviemvongsak, D. Monceau, C. Desgranges, B. Macquaire, Intergranular oxidation of Ni-base alloy 718 with a focus on additive manufacturing, Corros. Sci. 170 (2020), 108684, https://doi.org/10.1016/j.corsci.2020.108684.

[35] T. Sanviemvongsak, D. Monceau, B. Macquaire, High temperature oxidation of IN 718 manufactured by laser beam melting and electron beam melting: effect of surface topography, Corros. Sci. 141 (2018) 127–145, https://doi.org/10.1016/j.corsci.2018.07.005.

[36] C. Hong, D. Gu, D. Dai, S. Cao, M. Alkhayat, Q. Jia, A. Gasser, A. Weisheit, I. Kelbassa, M. Zhong, R. Poprawe, High-temperature oxidation performance and its mechanism of TiC/Inconel 625 composites prepared by laser metal deposition additive manufacturing, J. Laser Appl. 27 (2015), S17005, https://doi.org/10.2351/1.4898647.

[37] C. Juillet, A. Oudriss, J. Balmain, X. Feaugas, F. Pedraza, Characterization and oxidation resistance of additive manufactured and forged IN718 Ni-based superalloys, Corros. Sci. 142 (2018) 266–276, https://doi.org/10.1016/j.corsci.2018.07.032.

[38] E. Sadeghimeresht , P. Karimi , P. Zhang , R. Peng , J. Andersson , L. Pejryd , S. Joshi , Isothermal Oxidation Behavior of EBM-Additive Manufactured Alloy 718 BT - Proceedings of the 9th International Symposium on Superalloy 718 & Derivatives: Energy, Aerospace, and Industrial Applications E. Ott X. Liu J. Andersson Z. Bi K. Bockenstedt I. Dempster J. Groh K. Heck P. Jablonski M. Kaplan D. Nagahama C. Sudbrack 2018 Springer International Publishing Cham 219 240.

[39] M.R. Condruz, G. Matache, A. Paraschiv, T. Badea, V. Badilita, High temperature oxidation behavior of selective laser melting manufactured IN 625, Metals 10 (2020), https://doi.org/10.3390/met10050668.

[40] K.O. Gunduz, A. Visibile, M. Sattari, I. Fedorova, S. Saleem, K. Stiller, M. Halvarsson, J. Froitzheim, The effect of additive manufacturing on the initial High temperature oxidation properties of RE-containing FeCrAl alloys, Corrosion Science 188 (2021), 109553, https://doi.org/10.1016/j.corsci.2021.109553.

[41] S. Parizia, G. Marchese, M. Rashidi, M. Lorusso, E. Hryha, D. Manfredi, S. Biamino, Effect of heat treatment on microstructure and oxidation properties of Inconel 625 processed by LPBF, J. Alloy. Compd. 846 (2020), 156418, https://doi.org/10.1016/j.jallcom.2020.156418.

[42] E.R. Lewis, M.P. Taylor, B. Attard, N. Cruchley, A.P.C. Morrison, M.M. Attallah, S. Cruchley, Microstructural characterisation and high-temperature oxidation of laser powder bed fusion processed Inconel 625, Mater. Lett. 311 (2022), 131582, https://doi.org/10.1016/j.matlet.2021.131582.

[43] G. de Leon Nope, G. Wang, J.M. Alvarado-Orozco, B. Gleeson, Role of elemental segregation on the oxidation behavior of additively manufactured alloy 625, JOM 74 (2022) 1698–1706, https://doi.org/10.1007/s11837-022-05200-8.

[44] D. Monceau, M. Vilasi, High temperature oxidation of additively manufactured structural alloys, JOM 74 (2022) 1659–1667, https://doi.org/10.1007/s11837-022-05198-z.

[45] M. Liu, W. jie Zheng, J. zhong Xiang, Z. gang Song, E. xiang Pu, H. Feng, Grain growth behavior of inconel 625 superalloy, J. Iron Steel Res. Int. 23 (2016) 1111–1118, https://doi.org/10.1016/S1006-706X(16)30164-9.

[46] K. Antony, N. Arivazhagan, Studies on energy penetration and marangoni effect during laser melting process, J. Eng. Sci. Technol. 10 (2015) 509–525.

[47] H. Kyogoku, T.-T. Ikeshoji, A review of metal additive manufacturing technologies: mechanism of defects formation and simulation of melting and solidification phenomena in laser powder bed fusion process, 19-00182-19-00182, Mechan. Eng. Rev. 7 (2020), https://doi.org/10.1299/mer.19-00182.

[48] S.A. Khairallah, A.T. Anderson, A. Rubenchik, W.E. King, Laser powder-bed fusion additive manufacturing: physics of complex melt flow and formation mechanisms of pores, spatter, and denudation zones, Acta Materialia 108 (2016) 36–45, https://doi.org/10.1016/j.actamat.2016.02.014.

[49] H. Buscail, R. Rolland, C. Issartel, F. Rabaste, F. Riffard, L. Aranda, M. Vilasi, Effects of water vapour on the oxidation of a nickel-base 625 alloy between 900 and 1,100 °C, J. Mater. Sci. 46 (2011) 5903–5915, https://doi.org/10.1007/s10853-011-5544-2.

[50] A.M. de Sousa Malafaia, R.B. de Oliveira, L. Latu-Romain, Y. Wouters, R. Baldan, Isothermal oxidation of Inconel 625 superalloy at 800 and 1000 °C: Microstructure and oxide layer characterization, Mater. Charact. 161 (2020), 110160, https://doi.org/10.1016/j.matchar.2020.110160.

[51] J. Colas, L. Charpentier, M. Balat-Pichelin, Oxidation in air at 1400 K and optical properties of inconel 625, FeCrAlloy and kanthal super ER, Oxid. Metals 93 (2020) 355–370, https://doi.org/10.1007/s11085-020-09959-6.

[52] D.J. Young, Effects of water vapour on the oxidation of chromia formers, Mater. Sci. Forum. 595–598 PA (2008) 1189–1197, https://doi.org/10.4028/www.scientific.net/msf.595-598.1189.

[53] A. Galerie, J.P. Petit, Y. Wouters, J. Mougin, A. Srisrual, P.Y. Hou, Water vapour effects on the oxidation of chromia-forming alloys, Mater. Sci. Forum 696 (2011) 200–205, https://doi.org/10.4028/www.scientific.net/MSF.696.200.

[54] D. Texier, E. Copin, A. Flores, J. Lee, M. Terner, H.U. Hong, P. Lours, High temperature oxidation of NiCrAlY coated Alloy 625 manufactured by selective laser melting, Surf. Coat. Technol. 398 (2020), https://doi.org/10.1016/j.surfcoat.2020.126041.

[55] M. Calandri, D. Manfredi, F. Calignano, E.P. Ambrosio, S. Biamino, R. Lupoi, D. Ugues, Solution treatment study of inconel 718 produced by SLM additive technique in view of the oxidation resistance, Adv. Eng. Mater. 20 (2018) 1–16, https://doi.org/10.1002/adem.201800351.

[56] T. Sand, C. Geers, Y. Cao, J.E. Svensson, L.G. Johansson, Effective reduction of chromium-oxy-hydroxide evaporation from Ni-base alloy 690, Oxid. Metals 92 (2019) 259–279, https://doi.org/10.1007/s11085-019-09935-9.

[57] L. Bataillou, L. Martinelli, C. Desgranges, S. Bosonnet, K. Ginestar, F. Miserque, Y. Wouters, L. Latu-Romain, A. Pugliara, A. Proietti, D. Monceau, Growth kinetics and characterization of chromia scales formed on Ni–30Cr alloy in impure argon at 700 °C, Oxid. Metals 93 (2020) 329–353, https://doi.org/10.1007/s11085-020-09958-7.

[58] E. Schmucker, V. Szczepan, L. Martinelli, C. Petitjean, P.J. Panteix, S. Ben Lagha, M. Vilasi, Kinetic modelling of Cr2O3 growth on a Ni-30Cr alloy in silicate melts, Corros. Sci. 175 (2020), 108873, https://doi.org/10.1016/j.corsci.2020.108873.

[59] J.A. Nychka, D.R. Clarke, Quantification of aluminum outward diffusion during oxidation of FeCrAl alloys, Oxid. Metals 63 (2005) 325–352, https://doi.org/10.1007/s11085-005-4391-4.

[60] R. Peraldi, D. Monceau, B. Pieraggi, Correlations between growth kinetics and microstructure for scales formed by high-temperature oxidation of pure nickel. II, Growth kinetics, Oxid. Metals 58 (2002) 275–295, https://doi.org/10.1023/A:1020102604090.

[61] A.H. Rosenstein, J.K. Tien, W.D. Nix, Void Formation in Inconel Ma-754 by high temperature oxidation., metallurgical transactions, A, Phys. Metall. Mater. Sci. 17 A (1986) 151–162, https://doi.org/10.1007/BF02644451.

[62] F. Seitz, On the porosity observed, Acta Metall. 1 (1953) 355–369.

[63] F. Aldinger, Controlled porosity by an extreme kirkendall effect, Acta Metall. 22 (1974) 923–928, https://doi.org/10.1016/0001-6160(74)90059-5.

[64] C. Desgranges, F. Lequien, E. Aublant, M. Nastar, D. Monceau, Depletion and voids formation in the substrate during high temperature oxidation of Ni-Cr alloys, Oxid. Metals 79 (2013) 93–105, https://doi.org/10.1007/s11085-012-9328-0.

[65] H. Svensson, P. Knutsson, K. Stiller, Formation and healing of voids at the metal-oxide interface in NiAl alloys, Oxid. Metals 71 (2009) 143–156, https://doi.org/10.1007/s11085-008-9132-z.

[66] D.J. Potter, H. Al-Badairy, G.J. Tatlock, M.J. Bennett, Void formation and filling under alumina scales formed on Fe-20Cr-5AI based alloys and coatings, oxidised at temperatures up to 1200°C, Mater. Corros. 59 (2008) 414–422, https://doi.org/10.1002/maco.200804124.

[67] Y. Shida, G.C. Wood, F.H. Stott, D.P. Whittle, B.D. Bastow, Intergranular oxidation and internal void formation in Ni-40% Cr alloys, Corros. Sci. 21 (1981) 581–597, https://doi.org/10.1016/0010-938X(81)90010-X.

[68] B.A. Pint, R. Pillai, S. Dryepondt, High Temperature Oxidation Lifetime Modeling of Commercial Wrought NiCr, in: CORROSION 2019, 2019.

[69] R. Sachitanand, J.E. Svensson, J. Froitzheim, The Influence of Cr evaporation on Long Term Cr depletion rates in ferritic stainless steels, Oxid. Metals 84 (2015) 241–257, https://doi.org/10.1007/s11085-015-9552-5.

[70] H. Asteman, J.E. Svensson, L.G. Johansson, Evidence for chromium evaporation influencing the oxidation of 304L: the effect of temperature and flow rate, Oxid. Metals 57 (2002) 193–216, https://doi.org/10.1023/A:1014877600235.

[71] D.J. Young, B.A. Pint, Chromium volatilization rates from Cr2O3 scales into flowing gases containing water vapor, Oxid. Metals 66 (2006) 137–153, https://doi.org/10.1007/s11085-006-9030-1.

[72] S. Dryepondt, B.P. Thiesing, G.J. Tatlock, A.R. Jones, Void formation during cyclic oxidation of oxide dispersion strengthened FeCrAl alloys, Mater. High Temp. 00 (2020) 1–9, https://doi.org/10.1080/09603409.2020.1771657.

[73] J.E. Harris, Vacancy injection during oxidation-a re-examination of the evidence, Acta Metallurgica 26 (1978) 1033–1041, https://doi.org/10.1016/0001-6160(78)90053-6.

[74] S. Cruchley, H.E. Evans, M.P. Taylor, M.C. Hardy, S. Stekovic, Chromia layer growth on a Ni-based superalloy: Sub-parabolic kinetics and the role of titanium, Corros. Sci. 75 (2013) 58–66, https://doi.org/10.1016/j.corsci.2013.05.016.

[75] H. Nagai, M. Okabayashi, Deleterious effect of Ti addition on the oxidation resistance of ni–20Cr alloy, Trans. Jpn. Instit. Metals 22 (1981) 691–698, https://doi.org/10.2320/matertrans1960.22.691.

[76] G.R. Holcomb, D.E. Alman, The effect of manganese additions on the reactive evaporation of chromium in Ni-Cr alloys, Scripta Materialia 54 (2006) 1821–1825, https://doi.org/10.1016/j.scriptamat.2006.01.026.

[77] F.H. Stott, G.C. Wood, Internal oxidation, Mater. Sci. Technol. 4 (1988) 1072–1078, https://doi.org/10.1179/mst.1988.4.12.1072.

[78] B. Li, B. Gleeson, Effects of silicon on the oxidation behavior of Ni-base chromia-forming alloys, Oxid. Metals 65 (2006) 101–122, https://doi.org/10.1007/s11085-006-9003-4.

[79] A. Vayyala, I. Povstugar, D. Naumenko, W.J. Quadakkers, H. Hattendorf, J. Mayer, A nanoscale study of thermally grown chromia on high-Cr ferritic steels and associated oxidation mechanisms, J. Electrochem.Soc. 167 (2020), 061502, https://doi.org/10.1149/1945-7111/ab7d2e.

[80] T. Sand, A. Edgren, C. Geers, V. Asokan, J. Eklund, T. Helander, J.E. Svensson, L. G. Johansson, Exploring the effect of silicon on the high temperature corrosion of lean FeCrAl Alloys in humid air, Oxid. Metals 95 (2021) 221–238, https://doi.org/10.1007/s11085-020-10019-2.

[81] D.L. Douglass, J.S. Armijo, The effect of silicon and manganese on the oxidation mechanism of Ni-20 Cr, Oxid. Metals 2 (1970) 207–231, https://doi.org/10.1007/BF00603657.

[82] S.V. Divinski, G. Reglitz, G. Wilde, Grain boundary self-diffusion in polycrystalline nickel of different purity levels, Acta Mater. 58 (2010) 386–395, https://doi.org/10.1016/j.actamat.2009.09.015.